

Simulation of the Dissipative Dynamics of Strongly Interacting NV Centers with Tensor Networks

Jirawat Saiphet* and Daniel Braun

Institut für Theoretische Physik, Eberhard Karls Universität Tübingen, 72076 Tübingen, Germany

(Dated: November 25, 2024)

NV centers in diamond are a promising platform for highly sensitive quantum sensors for magnetic fields and other physical quantities. The quest for high sensitivity combined with high spatial resolution leads naturally to dense ensembles of NV centers, and hence to strong, long-range interactions between them. Hence, simulating strongly interacting NVs becomes essential. However, obtaining the exact dynamics for a many-spin system is a challenging task due to the exponential scaling of the Hilbert space dimension, a problem that is exacerbated when the system is modelled as an open quantum system. In this work, we employ the Matrix Product Density Operator (MPDO) method to represent the many-body mixed state and to simulate the dynamics of an ensemble of NVs in the presence of strong long-range couplings due to dipole-dipole forces. We benchmark different time-evolution algorithms in terms of numerical accuracy and stability against time evolution based on exact numerical diagonalization. Subsequently, we simulate the dynamics in the strong interaction regime, and study the impact of decoherence on the accuracy of the MPDO method. Lastly, we investigate the dynamics of quantum Fisher information and discuss under what circumstances a strong interaction can improve sensitivity for magnetic field sensing.

I. INTRODUCTION

Probing magnetic fields with high sensitivity and resolution is important in frontier research applications. A single NV-center (NV for short) in diamond has been proposed as a nanoscale probe [1] and used for measuring a magnetic field [2, 3]. Recently, controlled systems of double and triple NV centers were successfully fabricated [4]. Using NV ensembles with many spins has the potential to increase the sensitivity by having more spins in a probe. [5–7]. Requesting at the same time high spatial resolution leads to ensembles with high density. The resulting strong dipole-dipole interactions between the NVs lead, however, to a rapid population of sub-spaces of Hilbert space with reduced total spin. E.g., if we had two spins-1/2, not only the triplet states would get populated, but also the anti-symmetric singlet state, resulting in a reduced response to the applied magnetic field. This can be considered a form of intrinsic decoherence [8] in addition to the remaining external decoherence mechanisms, resulting in short coherence times [9] and hence less sensitivity. Decoupling the interactions with specific control pulses, or engineering the alignments of NVs to reduce interactions can increase the coherence time and sensitivity [8, 10, 11]. However, ideally one would like to profit from the interactions for generating entangled states that could highly enhance the sensitivity of the probe.

To model and optimize entanglement generation in a dissipative system with strong and long-range interactions, simulations of its dynamics in the presence of microwave control pulses is necessary. However, given the many-body nature of an ensemble, simulating its exact

dynamics is intractable. Exact simulations of closed spin-1/2 systems with long-range interaction have been implemented up to 32 spins [8, 12–14], and up to 12 spins with dissipation [15, 16]. In order to address this challenge, we use a tensor network approach to capture the dynamics of the ensemble. Matrix Product States (MPS) [17–20] were proposed for the efficient simulation of quantum metrology [21] and open quantum systems [22]. Simulation of non-Markovian systems has been performed using Matrix Product Operators (MPO) with a nearest-neighbors model [23, 24].

In this work, we consider an NV ensemble that consists of spin-1 particles. All NVs interact with each other by long-range dipole-dipole interaction. We simulate the dissipative dynamics by using the Matrix Product Density Operator (MPDO) method. We investigate the efficiency of using MPDO in simulating dynamics in the strong interaction limit and under dissipation. Operator entanglement entropy (opEE) is computed and used to demonstrate the interplay between strong interaction and dissipation for the capability of the MPDO to approximate the exact states. We then address and quantify possible sensitivity improvements from NV-NV interactions during the time evolution using quantum Fisher information.

II. THEORY

A. Strongly interacting NVs

An NV-center is a spin-1 system that forms in a carbon lattice of diamonds if two adjacent carbons are replaced by a nitrogen atom and a vacancy. Without an external field applied, the diamond structure creates a Zero Field Splitting (ZFS). Energy levels corresponding to states $|0\rangle$ and $|\pm 1\rangle$, with $m_s = 0, \pm 1$, respectively, are separated

* jirawat.saiphet@uni-tuebingen.de

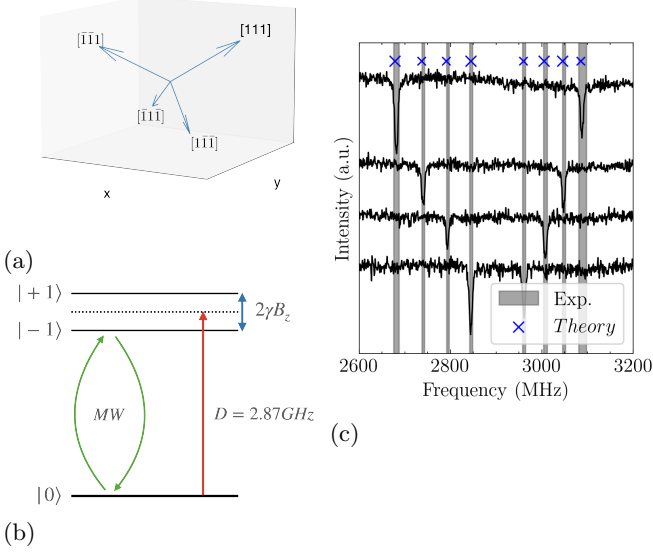


FIG. 1: (a) 4 possible orientations given by diamond's crystallographic axes. (b) Energy levels of an NV center. (c) ODMR spectra of 4 different axes from measurements and analytic calculations.

by $D = 2\pi \times 2870$ MHz.

Diamond's crystallographic axes provide 4 possible orientations of the principal axes of the NV, see Fig. 1a, separating them into different groups. E.g. the NV in [111] group has \hat{z} parallel with a unit vector $\frac{1}{\sqrt{3}}(1, 1, 1)$. Different groups have different couplings to a magnetic field, which leads to different energy levels that can be distinguished by optically detected magnetic resonance (ODMR).

In an external magnetic field, the field component B_z along the NV's principal axis creates an additional energy splitting between $|-1\rangle$ and $|+1\rangle$ proportional to B_z . This allows selective transitions from the ground state $|0\rangle$ to one of the two excited states by applying a microwave field at resonance frequency. Here we restrict ourselves to a transition to $|-1\rangle$.

The Hamiltonian for an individual NV with microwave drive with Rabi frequency $\Omega(t)$ is given by

$$\hat{H}_{NV,i} = \hbar \left(D\hat{S}_z^2 + g_s\mu_B B_z^{(i)}\hat{S}_z + \Omega(t) \cos(\omega t)\hat{S}_x^{(i)} \right), \quad (1)$$

where $g_s \simeq 2$ and μ_B the Bohr magneton. The spin operators for $S = 1$ are

$$\hat{S}_x = \frac{1}{\sqrt{2}} \begin{pmatrix} 0 & 1 & 0 \\ 1 & 0 & 1 \\ 0 & 1 & 0 \end{pmatrix}, \hat{S}_y = \frac{i}{\sqrt{2}} \begin{pmatrix} 0 & -1 & 0 \\ 1 & 0 & -1 \\ 0 & 1 & 0 \end{pmatrix}, \quad (2)$$

$$\hat{S}_z = \begin{pmatrix} 1 & 0 & 0 \\ 0 & 0 & 0 \\ 0 & 0 & -1 \end{pmatrix}.$$

Applying the unitary $\hat{U} = e^{i\omega t\hat{S}_z^2}$ to Eq. (1) to transform to a frame co-rotating with the microwave and using rotating-wave approximation (RWA) yields

$$\hat{H}_{NV,i} = \hbar \left((D - \omega)\hat{S}_z^2 + g_s\mu_B B_z^{(i)}\hat{S}_z + \frac{\Omega(t)}{2}\hat{S}_x^{(i)} \right). \quad (3)$$

At resonance frequency, $\omega = D \pm g_s\mu_B B_z^{(i)}$, the microwave drive makes a transition between $|0\rangle \leftrightarrow |\pm 1\rangle$ for the i -th NV. The energy levels of $\hat{H}_{NV,i}$ are depicted in Fig. 1b. They agree with the experimental observation [4].

NVs interact with each other via dipole-dipole interaction. We consider a case of strong interaction between NVs and hence ignore nuclear spin. The general definition of dipole-dipole interaction between NV- i and NV- j is

$$H_{\text{dip},ij} = -\frac{\mu_0(g_s\mu_B)^2\hbar^2}{4\pi r_{ij}^3} (3(\vec{S}^{(i)} \cdot \hat{r})(\vec{S}^{(j)} \cdot \hat{r}) - \vec{S}^{(i)} \vec{S}^{(j)}), \quad (4)$$

where $\vec{S}^{(i)} = (\hat{S}_x, \hat{S}_y, \hat{S}_z)^{(i)}$ are spin operators of NV- i , and $\hat{r}_{ij} = (r_x, r_y, r_z)_{ij}$ are the unit vectors connecting the two NVs. We restrict ourselves to the case where all NV centers have the same orientation. The dipole-dipole interaction in the rotating frame can then be transformed into an effective Hamiltonian [16],

$$\hat{H}_{\text{eff},\{ij\}} = C_{\text{dip}} \left(\frac{1}{2}(\hat{S}_x^{(i)}\hat{S}_x^{(j)} + \hat{S}_y^{(i)}\hat{S}_y^{(j)}) - \hat{S}_z^{(i)}\hat{S}_z^{(j)} \right) \quad (5)$$

where $C_{\text{dip}} = \frac{J_0 q_{ij}}{r_{ij}^3}$, $J_0 = \frac{\mu_0\hbar^2(g_s\mu_B)^2}{4\pi} = 2\pi \times 52 \text{ MHz} \cdot \text{nm}^3$, $q_{ij} = 3(\hat{r}_{ij} \cdot \hat{z}_i)(\hat{r}_{ij} \cdot \hat{z}_j) - \hat{z}_i \cdot \hat{z}_j$, with \hat{z}_i the unit vector pointing in direction of dipole i . It reduces to $q_{ij} = (3\cos^2\theta - 1)$ and $\cos\theta \equiv \hat{z}_i \cdot \hat{r}_{ij}$ in the case of the same group ($\hat{z}_i = \hat{z}_j$).

B. Tensor network state

Due to the r^{-3} scaling, the interactions within an ensemble of NVs extends beyond the nearest-neighbors and becomes long-range. These all-to-all interactions increase complexity and limit our capability to exactly simulate the system to only a few spins. To simulate the many-body dynamics for an ensemble of NVs, we represent the quantum state as a tensor network state. The state of a closed system is decomposed into a 1-dimensional tensor network structure, called Matrix Product State (MPS) [17–20],

$$|\Psi\rangle = \sum_{i_1 \dots i_N=1}^d A^{i_1} A^{i_2} \dots A^{i_N} |i_1 \dots i_N\rangle, \quad (6)$$

where a matrix A^{i_n} has matrix elements $A_{\alpha_{(n-1)}\alpha_n}^{i_n}$. The MPS decomposition in Eq. (6) can be visualized by a tensor diagram in Fig. 2a where each sphere visualizes

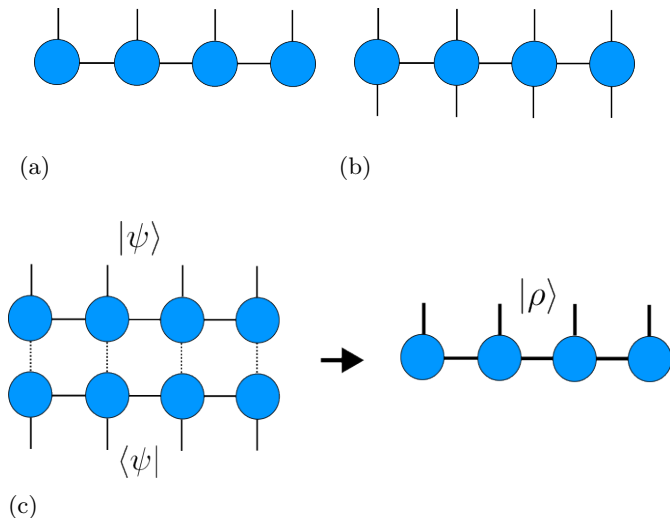


FIG. 2: Tensor diagrams representing (a) MPS: a wavefunction for a pure state, (b) MPO: an operator, and (c) MPDO: a vectorized density operator constructed from an MPS and its conjugate by contracting auxiliary indices, depicted as dash lines, and combining corresponding physical (bonds) indices. The thick line implies squared dimensions compared to the original index.

a tensor A^{i_n} and lines are indices of the tensors. The connecting lines represent a contraction by summation over a shared index of two tensors. Each matrix elements $A_{\alpha_{(n-1)}\alpha_n}^{i_n}$ in the MPS contains a physical index, i_n representing the local Hilbert space of the n^{th} NV. The virtual index, or bond index α_n having bond dimensions $d(\alpha_n) = \chi_n$ (except for $d(\alpha_0) = d(\alpha_N) = 1$) labels links between two tensors. Those linked bonds will be contracted when we extract any observable from the MPS. For example, the contraction of a shared index between tensors $A^{i_{n-1}} A^{i_n} \equiv \sum_{\alpha_{(n-1)}=1}^{\chi_{(n-1)}} A_{\alpha_{(n-2)}\alpha_{(n-1)}}^{i_{n-1}} A_{\alpha_{(n-1)}\alpha_n}^{i_n}$ happens between the left bond index α_{n-1} of A^{i_n} and the right bond index α_{n-1} of $A^{i_{n-1}}$. Note that in Eq. (6) we use notation where the summation over the α_n are not written explicitly, and $n = 1, \dots, N$. Physically, the bond dimension contains information about the entanglement entropy between the two parts of the tensor network that the bond connects. Using MPS allows us to compress the bond dimensions and to efficiently represent the ground state in compact, small Hilbert spaces.

A similar tensor network structure can be adapted to simulate an open system [25, 26]. To represent an operator we need a Matrix Product Operator (MPO) as given in Fig. 2b. This MPO, in an orthogonal basis, represents a density operator of the system,

$$\hat{\rho} = \sum_{i_1 \dots i_N=1}^d \sum_{i'_1 \dots i'_N=1}^d B^{i_1 i'_1} B^{i_2 i'_2} \dots B^{i_N i'_N} |i_1 \dots i_N\rangle \langle i'_1 \dots i'_N|. \quad (7)$$

For pure states, this MPO can be constructed by contracting auxiliary indices of two MPS and then combining corresponding physical (bond) indices. Furthermore, we combine the physical indices to create a Matrix Product Density Operator (MPDO) representing a vectorized density operator.

$$|\rho\rangle\rangle = \sum_{j_1 \dots j_N=1}^{d^2} B^{j_1} B^{j_2} \dots B^{j_N} |j_1 \dots j_N\rangle\rangle. \quad (8)$$

Here, $j_n = (i_n, i'_n)$ and $|j_n\rangle \in \mathbb{C}^{d^2}$ is combined from two physical indices. The dimension of each resulting index is doubled compared to the MPS. A graphical representation of this process is shown in Fig. 2c

C. Simulation of dissipative dynamics

We simulate ρ directly, including dissipation, by solving the vectorized master equation

$$\frac{\partial}{\partial t} |\rho\rangle\rangle = \mathcal{L} |\rho\rangle\rangle, \quad (9)$$

where $|\rho\rangle\rangle$ is the MPDO given by Eq. (8), and \mathcal{L} is a vectorized Lindblad operator defined as

$$\begin{aligned} \mathcal{L}(t) = & -i(\hat{H}(t) \otimes \mathbb{I} - \mathbb{I} \otimes \hat{H}^T(t)) \\ & + \sum_i \gamma_i [L_i \otimes (L_i^\dagger)^T - \frac{1}{2}(L_i^\dagger L_i \otimes \mathbb{I} + \mathbb{I} \otimes (L_i^\dagger L_i)^T)]. \end{aligned} \quad (10)$$

Note that when $\gamma_i = 0$, the dynamics are unitary. In this case when MPS is sufficient to simulate the system, utilizing MPDO is unnecessary and computationally more expensive due to the squared memory.

III. RESULTS

We simulate a 1-dimensional spin-1 chain with long-range interaction and dissipation using MPDO. We assume uniform separation for nearest neighbor spins, $r_{i,i+1} = r$ for any $i = 1, 2, \dots, N$. All spins align on the xy -plane such that the position $\vec{r}^{(i)} = r(i, i, 0)/\sqrt{2}$. For the very strong interaction regime, this separation is set to be $r < 2$ nm while experiments with dense samples have reached $r \sim 5$ nm [4]. In our simulations we use the following conditions: *i*) The amplitude of external magnetic field is chosen to match the level splitting read-off from the top line in Fig. 1c, $2g_s \mu_B B_z = 2\pi \times 407$ MHz. *ii*) Uniform Rabi frequency $\Omega(t) = \Omega = 2\pi \times 2.00$ MHz for driving the $|0\rangle \leftrightarrow |-1\rangle$ transition, $\omega = D - g_s \mu_B B_z$. *iii*) All NVs belong to the same orientation group parallel to [111]. *iv*) Time step $dt = 1$ ns. *v*) Initial state = $|0\rangle^{\otimes N}$.

A. Simulation algorithms in strong interaction regime without dissipation

Firstly, we investigate the precision and numerical stability of tensor network algorithms in the very strong interaction regime with $\gamma_i = 0$, for two different algorithms that simulate time-evolution and support the long-range model [27]: i) MPO W^{II} [28] and ii) time-dependent variational principle (TDVP) [29, 30]. We simulate dynamics of ensembles up to 10 NVs and $\chi_{\max} = 16$. Here χ_{\max} is a maximum dimension for all bonds. First of all, we investigate that the same dynamics are produced from both W^{II} and TDVP. This is shown as small discrepancy in the real part of $\langle S_z \rangle$ of the whole system produced by the two algorithms in Fig. 3b when $r = 2$ nm. However, the TDVP has significantly smaller errors in the imaginary parts, as shown in Fig. 3c. Furthermore, in Fig. 4 we observe that the W^{II} can be numerically unstable under certain condition i.e. when the interaction Hamiltonian is fully modeled by Eq. (4) and not being approximated by Eq. (5). The algorithm fails to produce a normalized value for expected magnetization $\langle S_z \rangle$ when the interaction strength becomes stronger while the TDVP is still valid compared to exact diagonalization. This is shown in Fig. 4 for $N = 3$ and $r = 0.5$ nm. We suspect that the observable divergence in W^{II} is a result of exploiting the complex time steps technique mentioned in [27] to improve the propagation error. As using the technique destroys unitarity of the propagator. However, without the technique, the numerical error of propagating the quantum state with W^{II} method compared to the exact evolution dramatically degrades from $\mathcal{O}(dt^2)$ to $\mathcal{O}(dt)$. In this case, the algorithm would not be able to capture the correct dynamics even in the weaker interaction regime. To avoid this problem, we keep the TDVP as the main algorithm for our simulations.

B. Dissipative dynamics with finite bond dimension

A major source of error when using MPS/MPDO is truncation error. Keeping finite bond dimensions and truncating when the bond indices exceed χ_{\max} introduces an error. This error is given by the square root of the sum of squares of the truncated singular values of all bonds,

$$\epsilon = \sqrt{\sum_{k > \chi_{\max}} (s_k)^2}. \quad (11)$$

Typically, these errors remain bounded if the state has entanglement that follows an area-law, e.g. when the system has only nearest-neighbor interactions. In such a case, the bond dimension grows with small singular values during the time evolution, allowing the simulation of large systems with small error. However, since we are considering a case of long-range interaction, this argument should not hold. In Fig. 5 and Fig. 6 we plot simulation results for different χ_{\max} with $r = 2.0$ nm and

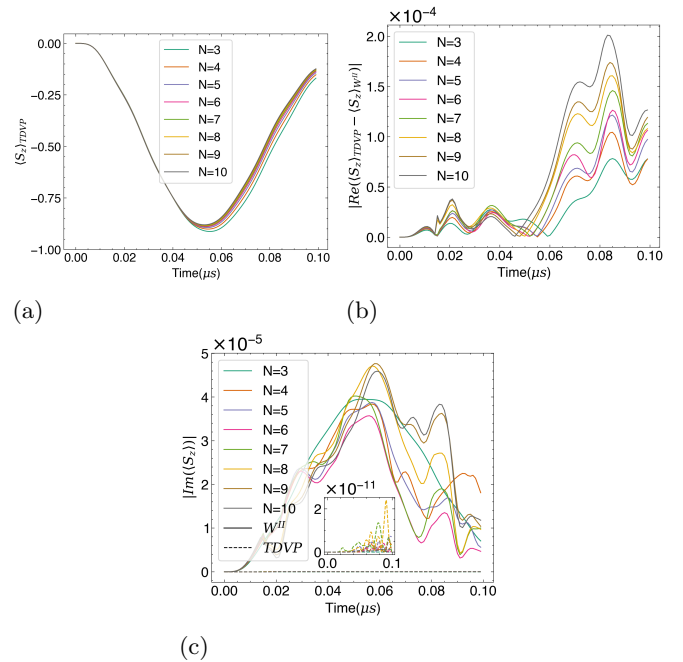


FIG. 3: Comparison of simulation results between W^{II} and TDVP algorithms for different N . (a) Real-time evolution of $\langle S_z \rangle$ calculated from TDVP algorithm with MPDO. (b) difference in real part of $\langle S_z \rangle$ from TDVP and W^{II} algorithms. (c) Numerical errors in imaginary part of W^{II} algorithm (main plot) are 5 orders of magnitude larger than in the TDVP algorithm (inset).

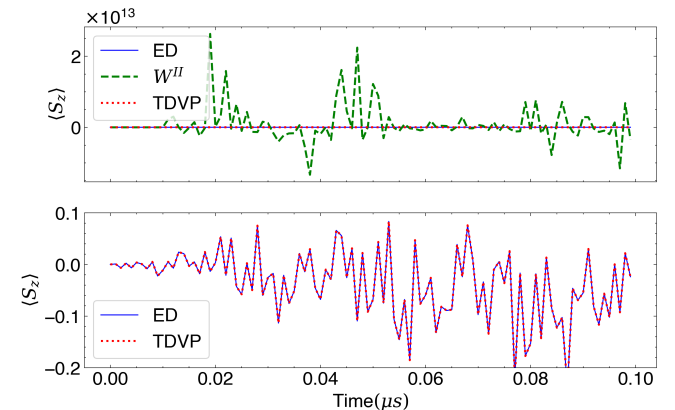


FIG. 4: W^{II} can fail when interaction becomes very strong (see top panel) while TDVP gives the same dynamics as exact diagonalization (bottom panel). Results from $N = 3$ and $r = 0.5$ nm.

$r = 1.5$ nm, compared to a result from exact diagonalization for $N = 4, 7$. We find that stronger interactions introduce bigger errors in bond truncation. The results for smaller χ_{\max} only follow the exact calculation as long as entanglement entropy does still not reach χ_{\max} ; i.e. up to a certain number of timesteps before diverging and becoming inaccurate due to truncation errors.

These results imply that it requires bigger χ_{\max} to capture the dynamics in the presence of long-range, strong interactions, thus less efficiency of the MPS/MPDO method.

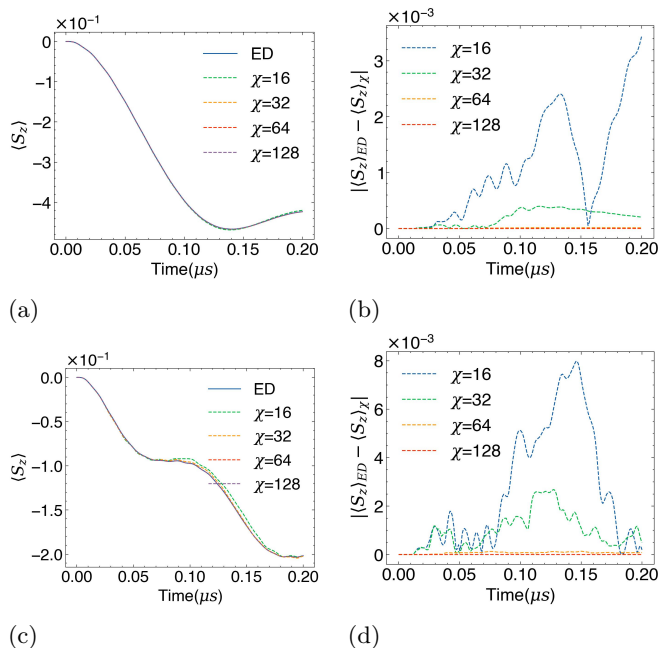


FIG. 5: 4NVs with $\gamma = 0$. (a) Average magnetization extracted from MPDO as a function of time and (b) numerical errors compared to exact diagonalization as a function of maximum bond dimension for $r = 2.0\text{ nm}$. (c), (d) for 1.5 nm

Next, we add dissipation by setting $\gamma_i = \gamma \neq 0$. So each spin has the same dissipation rate. Numerical values of γ are given in $(\mu\text{s})^{-1}$ units throughout. For the dissipation operator \hat{L}_i we choose the dephasing operator, $\hat{L}_i = \hat{S}_z$, relevant, e.g., for magnetic field noise. Fig. 7 shows the absolute errors compared to exact calculations of dissipative dynamics for different χ_{\max} and different values of r and γ . As a result, the discrepancy of these dissipative dynamics compared to the exact one is smaller than in the non-dissipative case for the same χ_{\max} . When the growth of singular values of bi-partition of the total state across the bond is limited by a larger γ , bond truncation becomes more effective since it introduces less errors. This demonstrates the interplay between the growth of entanglement entropy due to interactions and dissipation that hinders it. To understand quantitatively how stronger interactions induce entanglement entropy during time-evolution, we calculate the Operator Entanglement Entropy (opEE) of the reduced density matrix determined by cutting the system into two halves at the middle bond and tracing out the other half. We use the von Neuman entropy defined as

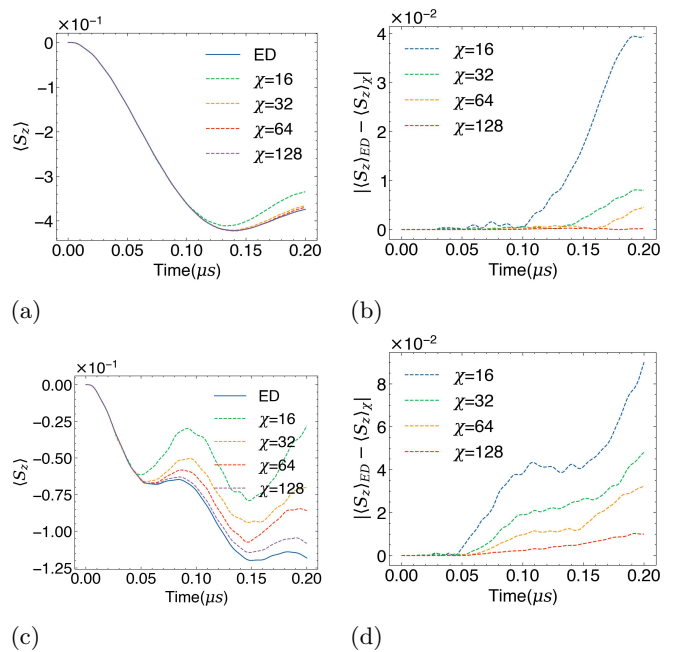


FIG. 6: 7NVs with $\gamma = 0$. (a) Average magnetization extracted from MPDO as a function of time and (b) numerical errors compared to exact diagonalization as a function of maximum bond dimension for $r = 2.0\text{ nm}$. (c), (d) for 1.5 nm

[31]

$$S_{op} = - \sum_i^{\chi} (\lambda_i)^2 \log_2 (\lambda_i)^2, \quad (12)$$

where λ_i are singular values of the cut bond with bond dimension χ for the vectorized operator. Here the λ_i are squared because they are singular values of a vectorized operator $|\rho\rangle$. Note that in general opEE does not give a direct measure of entanglement for mixed states. The opEE for a pure state is twice the value of its standard entanglement entropy, $S_{op}(|\psi\rangle) = 2S(|\psi\rangle)$, when $\rho = |\psi\rangle\langle\psi|$ [32]. Yet, the opEE provides insight into how well the state can be approximated by an MPDO, indicating simulation errors from a truncation [33].

After time-evolution, the middle bond index $\alpha_{(N/2+1)}$ which is the bond that equally separates the MPDO into two halves has the largest dimension. Fig. 8 shows the time evolution of opEE calculated from cutting the middle bond for $N = 4$ and $N = 7$. Figs. 8a and 8b are for $\gamma = 0$, Figs. 8c and 8d are for the different values of γ . The opEE growth as function of time is accelerated as interactions become stronger. This agrees with results of larger errors from truncation shown earlier. Except at very strong interaction, i.e. for $r = 1.5\text{ nm}$, opEE grows at the beginning and saturates rapidly. For $r = 1.5\text{ nm}$, the initial growth is fastest, but continues to grow after short time interval of relatively stable value around $0.12\mu\text{s}$. This behavior depends on the Rabi frequency Ω .

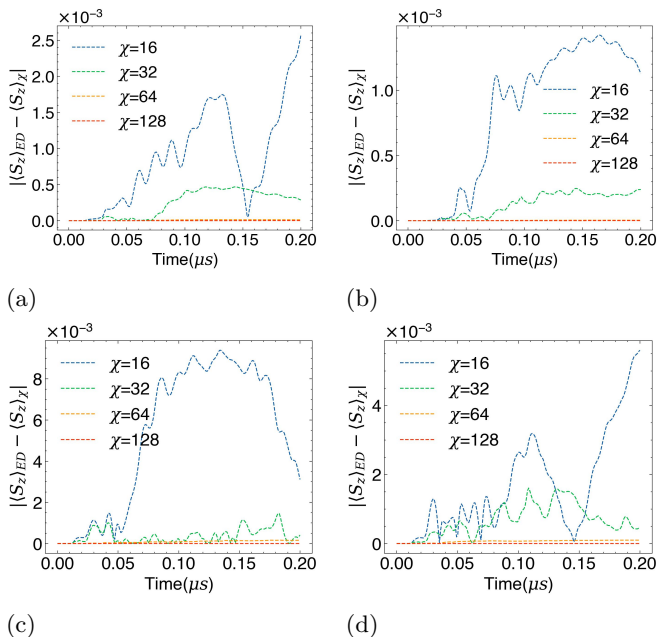


FIG. 7: Numerical errors compared to exact diagonalization as a function of maximum bond dimension for 4NVs. (a) $r = 2.0$ nm, $\gamma = 1.0$, (b) $r = 2.0$ nm, $\gamma = 5.0$, (c) $r = 1.5$ nm, $\gamma = 1.0$, (d) $r = 1.5$ nm, $\gamma = 5.0$.

The doubling Ω from $(2\pi)2$ MHz to $(2\pi)4$ MHz, the initial rise of opEE becomes even faster but the plateau is reached around $0.12\mu s$. See Fig. 11a in appendix.

C. QFI and sensitivity

According to the Cramér-Rao bound, the sensitivity in the estimation of a parameter θ using quantum probes is bounded by the inverse of the Quantum Fisher Information (QFI), $(\delta\theta)^2 \geq \frac{1}{MF_Q}$ where M is the number of independent measurements and F_Q is QFI [34]. The definition of QFI for a mixed state $\hat{\rho}$ is given by

$$F_Q = \text{Tr} \left[\hat{\rho} \hat{L}^2 \right], \quad (13)$$

where \hat{L} is the symmetric logarithmic derivative (SLD) that satisfies

$$\partial_\theta \hat{\rho} = \frac{1}{2} (\hat{L} \hat{\rho} + \hat{\rho} \hat{L}). \quad (14)$$

Hence, sensitivities can be improved by repeating the measurements or using more probes. For N independent probes, we obtain the Standard Quantum Limit (SQL), $\delta\theta \geq \mathcal{O}(1/\sqrt{N})$. However, the QFI can be increased when the probes are highly entangled. For example, under evolution with a pure Zeeman term, and in the absence of decoherence and dissipation, probes prepared in a GHZ state achieve optimal sensitivity for magnetic field

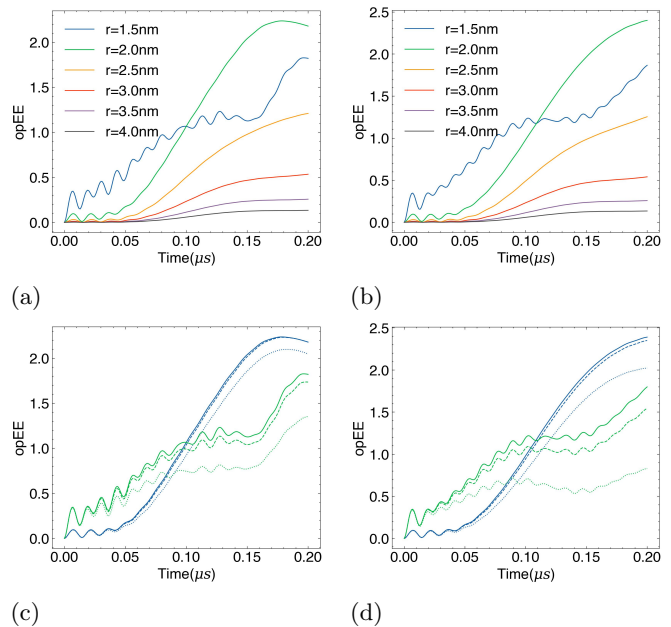


FIG. 8: Operator entanglement entropy (Eq. (12)) of middle bond. (a) and (b), for $N = 4$ and 7 respectively, show trends of opEE to grow faster when interactions get stronger. Each lines has $\gamma = 0$. (c) $N = 4$ and (d) $N = 7$, dissipation suppresses generation of opEE. Green: $r = 1.5$ nm, Blue: $r = 2.0$ nm. Line styles: solid ($\gamma = 0.0$), dashed ($\gamma = 1.0$), dotted ($\gamma = 5.0$).

measurement that follows the "Heisenberg limit" (HL), $\delta\theta \geq \mathcal{O}(1/N)$ [35].

Thus, since interactions are necessary for the creation of entanglement, dense NV ensembles harbor the potential for higher sensitivity compared to non-interacting NVs. However, the lack of permutational symmetry leads to the population of other irreducible representations of $SU(2)$ starting from the one with maximum spin, i.e. on average the total spin decays and sensitivity is reduced. Optimal control is therefore necessary to harvest the entanglement from strong interactions for achieving higher sensitivity.

D. Dynamics of QFI

To quantify the sensitivity of the ensemble of interacting NVs to a uniform magnetic field B_z , we compute the Quantum Fisher Information of the mixed state during time evolution. Instead of direct calculation using Eq. (13), we use the tensor network approach for calculating QFI as in [36]. Note that, unlike in the original work [36], we only optimize the SLD but not the input state ρ . In short, we iteratively search for the SLD that satisfies a definition of QFI:

$$F(\rho_\phi, L) = \sup_L [2\text{Tr}(\rho'_\phi L) - \text{Tr}(\rho_\phi L^2)]. \quad (15)$$

At the beginning, we randomly create the MPO approximation of an SLD, L , given by

$$L = \sum_{jk} \text{Tr}(S[1]_{k_1}^{j_1} \dots S[n]_{k_n}^{j_n}) |j\rangle \langle k|. \quad (16)$$

Here $S[l]_{k_l}^{j_l}$ is a Hermitian matrix. In searching for an optimal L we locally update $(S[1]_{k_1}^{j_1}, \dots, S[n]_{k_n}^{j_n})$ by sweeping from $S[1]$ to $S[n]$ and back to $S[1]$ again until F has converged. For example, when updating $S[l]_{k_l}^{j_l}$, all other tensors S_k^j are fixed and combined. Then after contractions, Eq. (15) becomes

$$F(\rho, L) = 2 \sum_{\alpha} b_{\alpha} S[l]_{\alpha} - 2 \sum_{\alpha\beta} S[l]_{\alpha} A_{\alpha\beta} S[l]_{\beta}. \quad (17)$$

Here, b and A are a vector and a matrix resulting from contracting the fixed tensors and combining the un-contracted indices. The diagrammatic explanation can be found on page 8 of [36]. Taking the derivative with respect to $S[l]$, $\partial F(\rho, L)/\partial S[l] = 0$, Eq. (17) yields $\frac{1}{2}(A + A^T)|S[l]\rangle = |b\rangle$. A solution to this equation provides a local extremum for the QFI. Since this local update approach tends to get stuck at local extrema, several repetitions with different initial L are needed and can be computationally expensive for large N .

Fig. 9 shows the dynamics of the QFI for a non-dissipative system with small size and different r . At each time step, we find the optimal SLD from 10 independent realizations and select the one with the largest QFI. Furthermore, we utilize the optimal SLD obtained from the previous time step as the initialization for the current time step. Based on our experience, although not guaranteed, implementing such a strategy can lead to a smoother result for the QFI.

According to the plots, the QFI of $r = 4.0$ nm nearly reaches values of N non-interacting probes, denoted as $F_{|+1\rangle^{\otimes N}} = N$. The QFI increases if the interactions are stronger, especially when $r \leq 2.5$ nm, leading to a QFI that can be greater than N . This suggests that the sensitivity for the probes is enhanced by the entanglement that is created by interaction. Still, as for opEE, the QFI remains relatively small when $r = 1.5$ nm, i.e. for very strong interaction. We find that this is due to an interaction strength of the nearest NV pairs ($C_{dip,(i,i+1)} = 2\pi \times 15.41$ MHz) that becomes substantially larger than the Rabi frequency ($\Omega = 2\pi \times 2.00$ MHz). As shown Fig. 10, the QFI can be further increased also for $r = 1.5$ nm by increasing the Rabi frequency.

IV. CONCLUSION

An ensemble of NV centers is a promising quantum metrology platform. While adding more independent spins improves the sensitivity, the probe can in principle also reach greater sensitivity due to entanglement created by interactions. Also, having a dense ensemble means

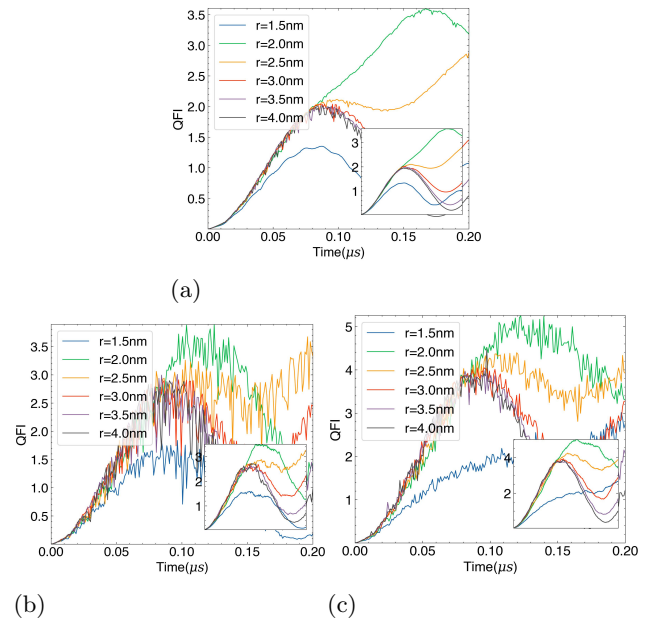


FIG. 9: Dynamics of QFI with Rabi frequency = $\Omega = 2\pi \times 2.00$ MHz. All plots are the best value computed from 10 different SLD initializations. The insets contain moving averages over 10 time steps. (a) $N = 2$, (b) $N = 3$, (c) $N = 3$.

that the total size of the probe can be smaller, resulting in better spatial resolution. However, without external control of the entanglement and the states generated, strong dipole-dipole interactions due to small separations between NV centers within a dense ensemble are usually detrimental for the sensitivity as they lead to a rapid decay of the total spin.

To investigate a system of strongly interacting NVs, we simulated the master equation with dissipation using MPDO. We benchmarked the W^{II} and the time-dependent variational principle (TDVP) algorithms against exact numerical diagonalization method for time evolution with a long-range interaction model. We found the W^{II} algorithm to have bigger errors in the imaginary part and to be less stable in a very small separation regime than TDVP. Then, with TDVP for small NV separations, we investigated the effect of finite maximum bond dimensions on the simulation accuracy. We again determined the accuracy as a function of bond dimensions by comparing the obtained states to those from exact diagonalization. Stronger interactions result in larger errors, suggesting the need for larger bonds. For dissipative dynamics, we found higher accuracy, which can be attributed to slower growth of operator entanglement entropy. These results indicate that the tensor network method can be suitable for simulating an open system. However, we find an exception for $r = 1.5$ nm, where the errors can be bigger even though the operator entanglement entropy is smaller than for $r = 2.0$ nm.

For applications in quantum sensing, we used the ap-

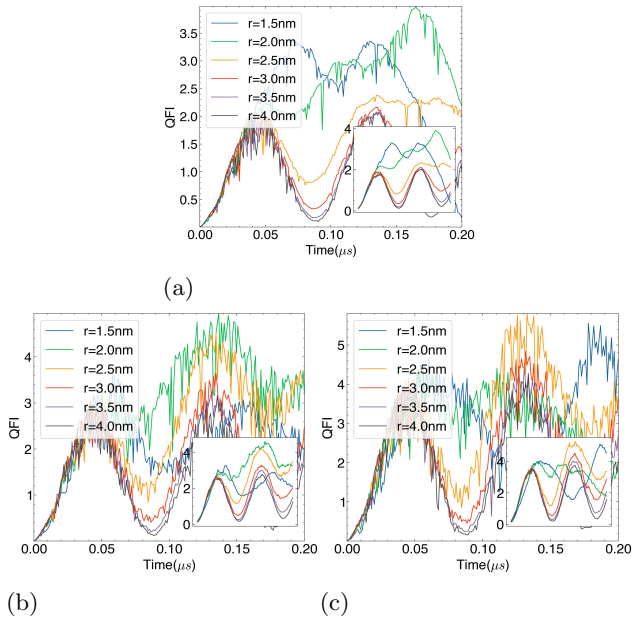


FIG. 10: Dynamics of QFI when the Rabi frequency is doubled from Fig. 9 to $2\Omega = (2\pi)4.00$ MHz. An increase of the maximal value of the QFI compared to the case with Rabi frequency $\Omega = 2\pi \times 2.00$ MHz can be observed for $r = 1.5$ nm. (a) $N = 2$, (b) $N = 3$, (c) $N = 4$.

proach of locally optimizing approximations of the SLD to obtain the quantum Fisher information. The QFI of driven ensembles shows that strong interaction can create entanglement-enhanced sensitivity compared to independent spins. Our results are based on quantum Fisher information, which gives the ultimate achievable sensitivity optimized over all possible POVM measurements and unbiased estimator functions of the parameter. Additional investigation will have to show to what extent this optimal sensitivity can be reached in specific sensing protocols.

Finally, we observed that the boost in sensitivity can diminish when the interaction becomes significantly larger than the Rabi frequency. In this situation, it is necessary to utilize microwaves with higher intensities for driving in order to increase the sensitivity.

Appendix A: Pure state entanglement entropy for a vector and an operator.

Any pure state has a Schmidt decomposition $|\psi_{AB}\rangle = \sum_i^r \sqrt{\lambda_i} |i\rangle_A \otimes |i\rangle_B$ with Schmidt coefficients $\sqrt{\lambda_i} > 0$ and $\sum_i^r \lambda_i = 1$. Then we can define the reduced density matrix for a bipartite system by partial trace over the other parts: $\rho_A = \text{Tr}_B[\rho_{AB}] = \sum_i^r \lambda_i |i\rangle_A \langle i|_A$ and $\rho_B = \text{Tr}_A[\rho_{AB}] = \sum_j^r \lambda_j |j\rangle_B \langle j|_B$. The density operator of the total system reads $\rho_{AB} = |\psi_{AB}\rangle \langle \psi_{AB}| = \sum_{i,j}^r \sqrt{\lambda_i} \sqrt{\lambda_j} (|i\rangle_A \otimes |i\rangle_B) \langle j|_A \otimes \langle j|_B$. The entangle-

ment entropy for reduced density operators is defined as

$$S(\rho_A) = -\text{Tr}[\rho_A \log(\rho_A)] = -\sum_{i=1}^r \lambda_i \log \lambda_i, \quad (\text{A1})$$

where $S(\rho_A) = S(\rho_B)$. To find the operator entanglement entropy (opEE), we vectorize $\rho_{AB} \rightarrow |\rho_{AB}\rangle\rangle$,

$$|\rho_{AB}\rangle\rangle = |\psi_{AB}\rangle |\psi_{AB}\rangle \quad (\text{A2})$$

$$= \sum_{\mu}^{r^2} \Lambda_{\mu} |i_A i_B; j_A j_B\rangle. \quad (\text{A3})$$

Here $\Lambda_{\mu} = \sqrt{\lambda_i} \sqrt{\lambda_j}$ and $\mu = (i, j)$. The super density operator, denoted by ρ^{\sharp} , can be created using an outer product:

$$\rho_{AB}^{\sharp} = |\rho_{AB}\rangle\rangle \langle \rho_{AB}| \quad (\text{A4})$$

$$= \sum_{\substack{\mu=(i,j), \\ \nu=(k,l)}}^{r^2, r^2} \Lambda_{\mu} \Lambda_{\nu} |i_A i_B; j_A j_B\rangle \langle k_A k_B; l_A l_B|. \quad (\text{A5})$$

Similar to $\rho_A(\rho_B)$, we can also have $\rho_A^{\sharp}(\rho_B^{\sharp})$; e.g. $\rho_A^{\sharp} = \sum_{\mu}^{r^2} \Lambda_{\mu}^2 |i_A; j_A\rangle \langle i_A; j_A|$. Then we can find the opEE,

$$S_{OP}(\rho_A^{\sharp}) = -\left[\sum_{\mu} \Lambda_{\mu}^2 \log(\Lambda_{\mu}^2) \right] \quad (\text{A6})$$

$$= -\left[\sum_{i,j} (\lambda_i \lambda_j) \log(\lambda_i \lambda_j) \right] \quad (\text{A7})$$

$$= -\left[\sum_{i,j} (\lambda_i \lambda_j) (\log(\lambda_i) + \log(\lambda_j)) \right] \quad (\text{A8})$$

$$= -\left[\sum_i (\lambda_i) \log(\lambda_i) \sum_j (\lambda_j) + \sum_i (\lambda_i) \sum_j (\lambda_j) \log(\lambda_j) \right] \quad (\text{A9})$$

$$= -\left[2 \sum_i \lambda_i \log(\lambda_i) \right] \quad (\text{A10})$$

$$= 2S(\rho_A). \quad (\text{A11})$$

Appendix B: opEE for Rabi frequency 2Ω

The operator entanglement entropy when the Rabi frequency is doubled from $\Omega = (2\pi)2.00$ MHz, hence $2\Omega = 2\pi \times 4.00$ MHz.

ACKNOWLEDGMENTS

This work was supported by the Baden Württemberg Stiftung, project CDINQUA. Tensor network codes are modified and implemented algorithms from TenPy [37].

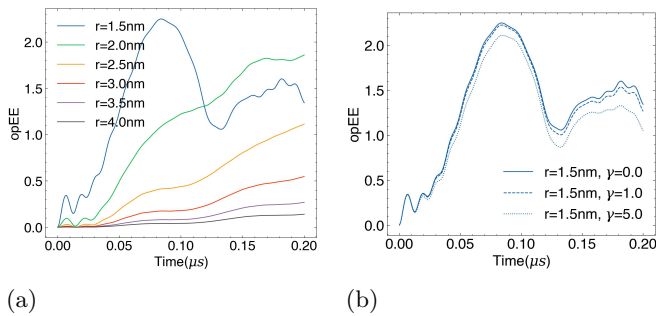


FIG. 11: Operator entanglement entropy of middle bond. Rabi frequency = 2Ω .

-
- [1] J. M. Taylor, P. Cappellaro, L. Childress, L. Jiang, D. Budker, P. R. Hemmer, A. Yacoby, R. Walsworth, and M. D. Lukin, *Nature Phys* **4**, 810 (2008), publisher: Nature Publishing Group.
- [2] P. Welter, J. Rhensius, A. Morales, M. S. Wörnle, C. H. Lambert, G. Puebla-Hellmann, P. Gambardella, and C. L. Degen, *Applied Physics Letters* **120**, 074003 (2022).
- [3] B. L. Dwyer, L. V. Rodgers, E. K. Urbach, D. Bluvstein, S. Sangtawesin, H. Zhou, Y. Nassab, M. Fitzpatrick, Z. Yuan, K. De Greve, E. L. Peterson, H. Knowles, T. Sumarac, J.-P. Chou, A. Gali, V. Dobrovitski, M. D. Lukin, and N. P. de Leon, *PRX Quantum* **3**, 040328 (2022).
- [4] M. Haruyama, S. Onoda, T. Higuchi, W. Kada, A. Chiba, Y. Hirano, T. Teraji, R. Igarashi, S. Kawai, H. Kawarada, Y. Ishii, R. Fukuda, T. Tani, J. Isoya, T. Ohshima, and O. Hanaizumi, *Nature Communications* 2019 10:1 **10**, 1 (2019), publisher: Nature Publishing Group.
- [5] P. Balasubramanian, C. Osterkamp, Y. Chen, X. Chen, T. Teraji, E. Wu, B. Naydenov, and F. Jelezko, *Nano Lett.* **19**, 6681 (2019), publisher: American Chemical Society.
- [6] H. Zheng, J. Xu, G. Z. Iwata, T. Lenz, J. Michl, B. Yavkin, K. Nakamura, H. Sumiya, T. Ohshima, J. Isoya, J. Wrachtrup, A. Wickenbrock, and D. Budker, *Phys. Rev. Appl.* **11**, 064068 (2019), publisher: American Physical Society.
- [7] C. Wang, Q. Liu, Y. Hu, F. Xie, K. Krishna, N. Wang, L. Wang, Y. Wang, K. C. Toussaint Jr, J. Cheng, H. Chen, and Z. Wu, Realization of high-dynamic-range broadband magnetic-field sensing with ensemble nitrogen-vacancy centers in diamond (2022), arXiv:2209.11360 [quant-ph].
- [8] H. Zhou, J. Choi, S. Choi, R. Landig, A. M. Douglas, J. Isoya, F. Jelezko, S. Onoda, H. Sumiya, P. Cappellaro, H. S. Knowles, H. Park, and M. D. Lukin, *Phys. Rev. X* **10**, 031003 (2020), publisher: American Physical Society.
- [9] E. Bauch, S. Singh, J. Lee, C. A. Hart, J. M. Schloss, M. J. Turner, J. F. Barry, L. M. Pham, N. Bar-Gill, S. F. Yelin, and R. L. Walsworth, *PHYSICAL REVIEW B* **102**, 134210 (2020).
- [10] D. Farfurnik, Y. Horowicz, and N. Bar-Gill, *Phys. Rev. A* **98**, 033409 (2018).
- [11] C. Osterkamp, M. Mangold, J. Lang, P. Balasubramanian, T. Teraji, B. Naydenov, and F. Jelezko, *Sci Rep* **9**, 5786 (2019), publisher: Nature Publishing Group.
- [12] A. W. Sandvik, *Phys. Rev. Lett.* **104**, 137204 (2010).
- [13] S. Schiffer, J. Wang, X.-J. Liu, and H. Hu, *Phys. Rev. A* **100**, 063619 (2019), publisher: American Physical Society.
- [14] C. Cheng, *Phys. Rev. B* **108**, 155113 (2023).
- [15] S. Essink, *Boundary-Driven XXZ Spin-1/2 Chain*, Ph.D. thesis, Universität Bonn, Bonn (2018).
- [16] G. Kucsko, S. Choi, J. Choi, P. C. Maurer, H. Zhou, R. Landig, H. Sumiya, S. Onoda, J. Isoya, F. Jelezko, E. Demler, N. Y. Yao, and M. D. Lukin, *Phys. Rev. Lett.* **121**, 023601 (2018).
- [17] G. Vidal, *Phys. Rev. Lett.* **91**, 147902 (2003), publisher: American Physical Society.
- [18] D. Perez-Garcia, F. Verstraete, M. M. Wolf, and J. I. Cirac, *Quantum Info. Comput.* **7**, 401–430 (2007).
- [19] U. Schollwöck, *Annals of Physics* January 2011 Special Issue, **326**, 96 (2011).
- [20] R. Orús, *Annals of Physics* **349**, 117 (2014).
- [21] M. Jarzyna and R. Demkowicz-Dobrzański, *Phys. Rev. Lett.* **110**, 240405 (2013).
- [22] R. Finsterhölzl, M. Katzer, A. Knorr, and A. Carmele, *Entropy* **22**, 984 (2020), number: 9 Publisher: Multidisciplinary Digital Publishing Institute.
- [23] A. W. Schlimgen, K. Head-Marsden, L. M. Sager, P. Narang, and D. A. Mazziotti, *Phys. Rev. Res.* **4**, 023216 (2022).
- [24] G. E. Fux, D. Kilda, B. W. Lovett, and J. Keeling, *Phys. Rev. Research* **5**, 033078 (2023).
- [25] H. Weimer, A. Kshetrimayum, and R. Orús, *Rev. Mod. Phys.* **93**, 015008 (2021).
- [26] D. Jaschke, S. Montangero, and L. D. Carr, *Quantum Science and Technology* **4**, 013001 (2018).
- [27] S. Paeckel, T. Köhler, A. Swoboda, S. R. Manmana, U. Schollwöck, and C. Hubig, *Annals of Physics* **411**, 167998 (2019).
- [28] M. P. Zaletel, R. S. K. Mong, C. Karrasch, J. E. Moore, and F. Pollmann, *Phys. Rev. B* **91**, 165112 (2015).
- [29] J. Haegeman, C. Lubich, I. Oseledets, B. Vandereycken, and F. Verstraete, *Phys. Rev. B* **94**, 165116 (2016), publisher: American Physical Society.

- [30] C. Hubig, J. Haegeman, and U. Schollwöck, Phys. Rev. B **97**, 045125 (2018).
- [31] S. Murciano, J. Dubail, and P. Calabrese, J. Phys. A: Math. Theor. **57**, 145002 (2024), publisher: IOP Publishing.
- [32] G. J. Preisser Beltrán, *Numerical studies of entanglement dynamics in open spin systems*, These de doctorat, Strasbourg (2023).
- [33] G. Preisser, D. Wellnitz, T. Botzung, and J. Schachenmayer, Phys. Rev. A **108**, 012616 (2023).
- [34] M. G. A. Paris, Int. J. Quantum Inform. **07**, 125 (2009), publisher: World Scientific Publishing Co.
- [35] V. Giovannetti, S. Lloyd, and L. Maccone, Science **306**, 1330 (2004), publisher: American Association for the Advancement of Science.
- [36] K. Chabuda, J. Dziarmaga, T. J. Osborne, and R. Demkowicz-Dobrzański, Nat Commun **11**, 250 (2020), number: 1 Publisher: Nature Publishing Group.
- [37] J. Hauschild and F. Pollmann, SciPost Phys. Lect. Notes , 5 (2018).